FACULTY OF SCIENCE
UNIVERSITY OF COPENHAGEN

Master Thesis

Sadik Acili

A galaxy illuminated by a GRB at z=2.33

Dark Cosmology Centre - The Niels Bohr Institute

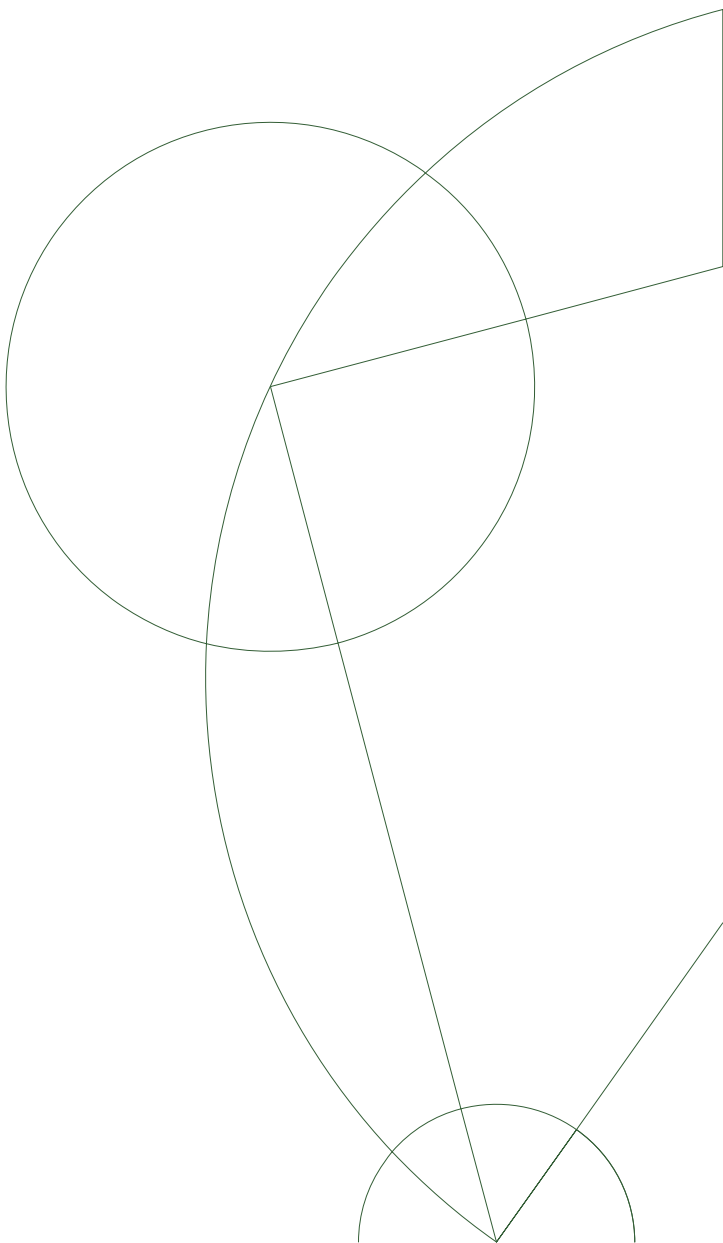

Supervisor: Johan P. U. Fynbo

30. November 2016

Abstract

This thesis is about the detection and analysis of a Gamma-Ray-Burst event taking place at a redshift of $z = 2.33$. The absorption-lines of the intervening galactic system is easily identified and their characteristics enables us to calculate some of the host-galaxy properties, such as the redshift, column densities and metallicities - one of the only ways possible using Gamma-Ray-Bursts as cosmological host-galaxy probes.

Chapter 1 is a brief introduction to Gamma-Ray-Bursts and their discovery, origin, progenitors and what they can do for us, along with a brief description of how to interpret the absorption-lines, how to measure the column densities and deploy the curve-growth-method to infer host-galaxy properties. Basically; showing what we can infer from a GRB spectrum.

A description and introduction to some key elements in our understanding of the Universe which we live in, will be presented in Chapter 2, starting with the Big Bang and the onset of the primordial nucleosynthesis, through the epoch of recombination, the radiation, matter and dark-energy dominated eras, all the way up to the formation of structure and what we can observe today. This chapter will hopefully form the framework in which we understand GRB's in a cosmological setting.

Chapter 3 is an introduction to spectral analysis, how to interpret the equivalent widths of an absorption line and relate it to the different optical regimes in a curve-of-growth analysis. The formulas behind the IDL-fitting procedures are outlined.

In Chapter 4 I will present the obtained data and the analysis including identifications of the host-galaxy atomic lines, column-densities and the metallicity of the host-galaxy. It turns out, the extremely bright oxygen emission-line from the host-galaxy itself is also present in the spectrum. This will be showed.

In the final Chapter 5 I will conclude and discuss my work comparing it with other high-redshift GRB studies and determine whether the obtained metallicities fits within the uncertainties in these other works. A full-scale χ^2 error-analyzation lies outside the scope of my thesis, but still a simple and somewhat crude error-margin to the metallicity can be given.

Acknowledgements

My first and foremost acknowledgment is to my supervisor, professor Johan P.U Fynbo, for his guidance and patience throughout the process of writing my thesis. Somehow he always found time to supervise while being burdened with lots of other work as well. Thank you Johan.

Thank you Anja C. Andersen for always helping me out when I was stuck somehow in my studies or with some obstacle in my life, study-related or not. Although not being directly part of this work you were never more distant than an e-mail, or a simple phone-call. "Never give up, never surrender" as you said to me one day, quoting an episode of Star Trek I have yet to watch.

Thanks to professor Jens Hjorth for creating such a great research center and atmosphere at Dark, full of great and sweet people always smiling at me in the hall-ways. I remember when the offices were a library I used to study and read at, today it is a world-class research center - and I was fortunate enough to be a very very very (very) small part of it.

Finally, last but not least, I'd like to thank my sister, my niece, my nephew and my father but especially my mother (a classic among turkish men I think). Annecim, you are amazing and I have no adequate words for my gratitude toward you.

This thesis is dedicated to you. Thank you for everything.

Sadik Acili
November 30 2016 - Copenhagen

Contents

Abstract **3**

Acknowledgements **5**

1 Introduction to Gamma Ray Bursts **13**
1.1 A brief history of GRBs 13
1.2 GRB progenitors 16

2 Standard Cosmology **19**
2.1 Introduction 19
2.2 Primordial nucleosynthesis 19
2.3 The redshift-relation 20
2.4 Evolution of the scale-factor 21
2.5 The temperature relation 23
2.6 Formation of structure 24

3 Theory **27**
3.1 Introduction to spectre 27
3.2 Formation of spectral lines 27
3.3 Line profiles 29
3.4 Line widths 29

4 Analyis of the GRB151021A spectrum **33**
4.1 The Data 33
4.2 Determining the redshift 34
4.3 DLA fitting 34
4.4 Column densities 35
4.5 Effective b-parameter fitting 35
4.6 Metallicity and relative abundances 41
4.7 Host galaxy search 41

5 Results and Conclusion **43**

Bibliography **46**

List of Tables

2.1 Equation of state parameters, scaling, energy-density and present day density parameters for the Benchmark Model. 22

4.1 UVB lines in the spectrum of the afterglow of GRB151021A 35
4.2 VIS lines in the spectrum of the afterglow of GRB151021A 36
4.3 Column density lower limit of selected weak lines 38
4.4 Column densities of selected ions using effective doppler parameter fits. . 40
4.5 Metallicities of selected elements 41

List of Figures

1.1 The first burst event recorded by the Vela 5 satellite on the 2. July 1967. Source: J. Bonell 14
1.2 2704 BATSE GRB observations uniformly distributed across the sky. Credit: BATSE/NASA 15
1.3 GRB lightcurves from BATSE showing the variability in the number of spikes, duration and countrates (Credit: NASA/BATSE) 17

3.1 Curve-of-growth and the relation between column density and equivalent width for different optical regimes (from Petitjean (1998)). The three inserts show the three different regimes: optically thin lines, the flat part of the Curve of growth with saturated lines, and finally lines that are saturated in the damping wings. 32

4.1 IDL fitting for the $\lambda_o = 6746.60$Å absorption line, which is a blend of lines from ZnII, CrII and CoII. 37
4.2 Fitting the column density of the DLA and the Lyman-β line. 37
4.3 SII-line effective b-parameter fitting. 38
4.4 SiII-line effective b-parameter fitting 39
4.5 NiII-line effective b-parameter fitting 39
4.6 FeII-line effective b-parameter fitting 40
4.7 The [OIII]-5006.843 line showing in the subtracted spectrum in the NIR region 42
4.8 The [OIII] emission line. 42

5.1 Metallicity-redshift distribution for a sample of GRB-DLAs at a specific reshift. 44
5.2 The metallicity/luminosity relation adopted in Fynbo et al. (2008) to model the metallicity distribution of GRB host galaxies. 44

Chapter 1

Introduction to Gamma Ray Bursts

1.1 A brief history of GRBs

Once upon a time...

... there was a nuclear arms race between U.S.A and the Sovjet Union. It had begun right after the end of the 2nd World War but within a few decades these two nations found themselves in another race - this time for the moon and space. The russians took the lead with the launch of Sputnik in 1957, followed up by its american counterparts Explorer 1 and Explorer 2 and various other satellites and space-missions from both sides in the following years. The basic purpose and the underlying idea was simple and terrifying; to be able to carry and deliver nuclear payloads with satellites, and obliterate the enemy - first.

The idea of venturing out to outer space and go where no other had gone before was a side-kick and discoveries would eventually be scientific spin-offs. The Cold War remained cold though, and to prevent any nuclear tests in outer space or behind the moon, where it would have gone about unnoticed, the Nuclear Test Ban Treaty was signed in 1963. But as elegantly formulated by Christina C. Thöne in her PhD-thesis, "trust is good, but control is better" Thöne (2008), the US government soon began to design and launch their first satellites, Vela I and Vela II, which would look for traces of a nuclear explosion - namely the γ-radiation from the decay of radioactive materials produced in the blast-waves of nuclear explosions. The program which had started in 1965 with primitive instruments soon got upgraded with Vela IV and Vela V and the first detection of a Gamma Ray Burst was about to happen soon.

First detection

The first Gamma Ray Burst (GRB670702) was recorded from the Vela V satellite the 2. of July 1967, Figure 1.1 and within a few weeks several more GRB-events was observed, coming from apparently different and random directions of the sky - the russians were not to blame. Having ruled out earthly origins the scientific observations could begin. The Interplanetary Network (IPN) was established in 1977, with the aim of being able to better localize the bursts, and the first large project specifically dedicated to study

GRBs was the Compton Gamma Ray Observatory (GRBO), with the BATSE (Burst And Transient Source Equipment) detector launched in 1991. During its 9-year operational life-time BATSE recorded several thousands of trigger-events and led to two very important discoveries. First of all; the GRBs were distributed uniformly across the sky, and they came in two main groups, short duration and long duration GRBs indicating a difference in their progenitors, Nature had apparantly two distinct ways of producing GRBs.

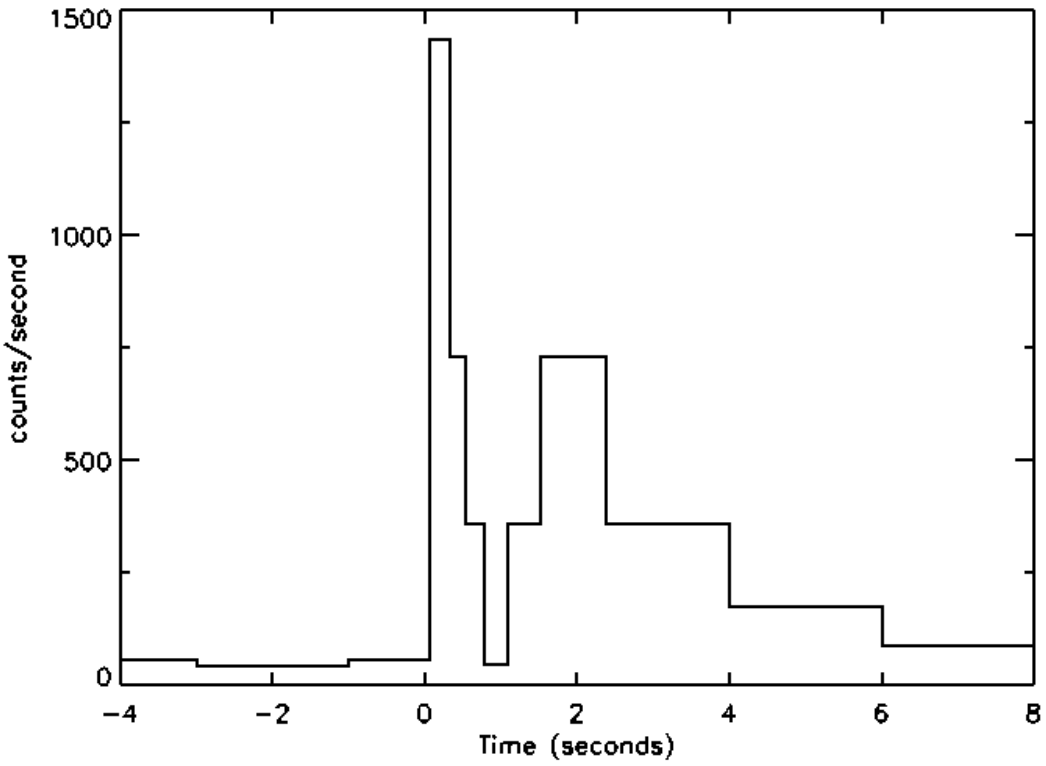

Figure 1.1: The first burst event recorded by the Vela 5 satellite on the 2. July 1967. Source: J. Bonell

During the time of BATSE, there was another great debate reminiscent of the Great Debate of the thirties, this time about whether the GRBs had a galactic or a cosmological origin advocated by Donald Lamb and Bohdan Paczynsky respectively. Even though the uniform distribution of GRBs across the sky was an indication of a cosmological origin, Figure 1.2, some astronomers were still clinging to the galactic-origin idea. Their ideas were based on the newly discovered neutron stars and pulsars in the Milky Way, showing to be uniformly distributed across the sky also. So even if GRBs had something to do with neutron stars and/or pulsars, with galactic origins, they would still appear to be uniformly distributed and therefore mimic a cosmological origin instead, hence the confusion.

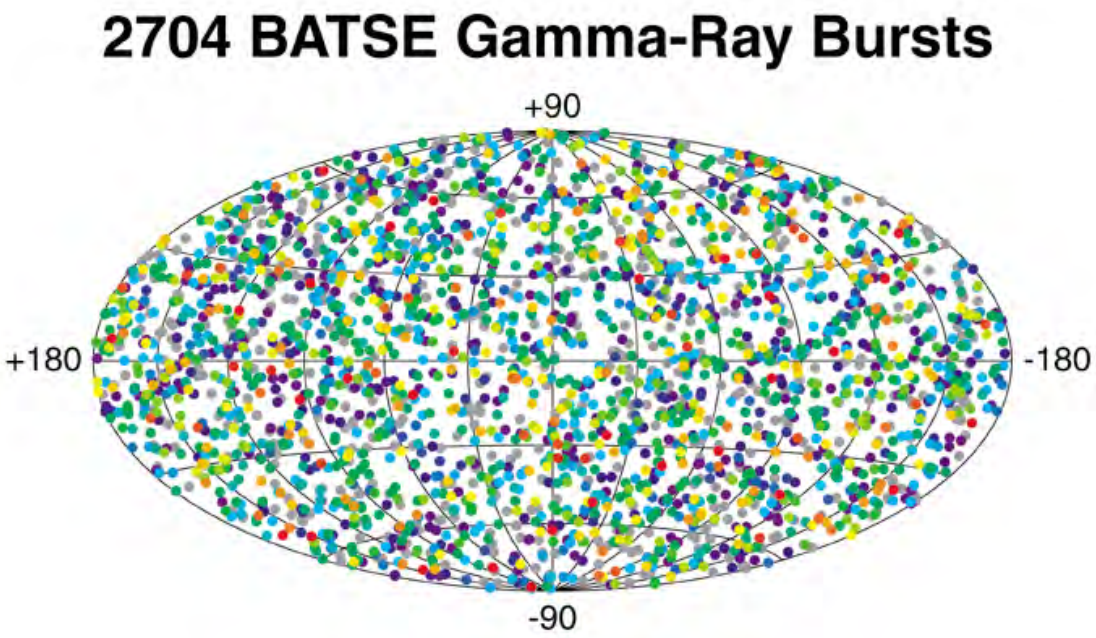

Figure 1.2: 2704 BATSE GRB observations uniformly distributed across the sky. Credit: BATSE/NASA

The question of the GRB origins were firmly answered Feb. 28 1997 (Costa et al. (1997)). The Italian BeppoSAX satellite detected a GRB, enabling ground based telescopes to quickly find and localize a lower-energy counterpart source in X-rays. Images taken with the William Herschel and Isaac Newton telescopes revealed that one of the objects in the field had faded when comparing images a week later. A host galaxy was eventually found and a spectrum showed a redshift of $z = 0.695$ - the second great debate had come to an, the GRBs had cosmological origins, coming from cosmological distances.

BeppoSAX also detected the first radio afterglow GRB970508 (Frail et al. (1997)) and later also what would be the first evidence of a connection between long-duration GRBs and supernovae, GRB980425 a long-duration GRB located in the spiral arm of a dwarf galaxy at $z = 0.0085$ (Galama et al. (1998)).

Observational build-up

With the most important questions about the origins of the GRBs answered, the aim was now to get a larger sample of afterglows observed in the entire wavelength range.

The Swift era began with the launch of the Swift satellite in 2004, purely designed for GRB detection and follow up spectroscopy Gehrels et al. (2009). It consisted of three instruments, the burst alert telescope (BAT) with an error box of 1-4 arcmin, the X-ray telescope (XRT) which could slew within a few seconds to the burst position, and the UV telescope (UVOT) with 3 UV and 3 optical filters with a range from 1700Å-6000Å, to detect the optical counterpart.[1]

On the 11. June 2008 the latest generation of a GRB detecting satellite was launched, the Fermi Gamma-ray Space Telescope (FGST) carrying two scientific instruments, the Large Area Telescope (LAT) and the Gamma-Ray Burst Monitor (GBM), with the intent of studying astrophysical and cosmological phenomena, such as active galactic nuclei, pulsars, other high-energy sources and dark matter (with the LAT), and to study GRBs (with the GBM). With the FGST the detection rate of GRBs would be around 200 pr. year, thus doubling the Swift satellite detection rate, and with energy ranges several times more intense than ever before, hopefully giving a better understanding of GRBs.

The future for GRB detection and observation looks bright and promising so far with FGST recently getting a 5-year mission extension, ending it in 2018. Looking even deeper into the future one can imagine the need for GRB-astronomy and GRB-observations will only increase due to the recent experimental verifications of gravitational waves (2015) and their connections with GRB-producing events in black hole or neutron star mergers. Having opened up another field with gravitational astronomy, with ever increasingly lookback-times, will also fuel the need for even more extensive GRB searches and surveys with the aim of probing the Universe at high-redshifts and studying the state of the very early universe.

1.2 GRB progenitors

From both BATSE and subsequent observations it was, as mentioned earlier, clear that the GRBs fell in two distinct categories; short and long GRBs with the short GRBs lasting shorter than 2 secs and long GRBs lasting in the order of 10 to 100s and longer. It was also clear that no two GRBs were identical. Figure 1.3 shows 12 examples from the BATSE sample. The light curves vary greatly in morphology. Some are very complex with many peaks indicating a somewhat complex progenitor system.

Actually a hint to the GRB progenitors was already given with the very first Vela I and Vela II satellites and their first GRB detections. How was it possible that a relatively crude satellite as the Vela I was able to detect GRBs so easily in the first place? The answer was lying in the energy-output of the GRBs and since they were also cosmological, the amount of energy released during such an event had to be immense, outshining the entire Universe for a very brief moment. GRBs were indeed the most powerful flashes of electromagnetic radiation since the Big Bang, and only a few types of objects could have such high energy-releases - supernovae or compact object mergers.

[1] The data used for this thesis stems from the Swift satellite distributed throughout the so-called Gamma-Ray burst Coordinate Network. `http://gcn.gsfc.nasa.gov`) with GRB151021A having the trigger #660671.

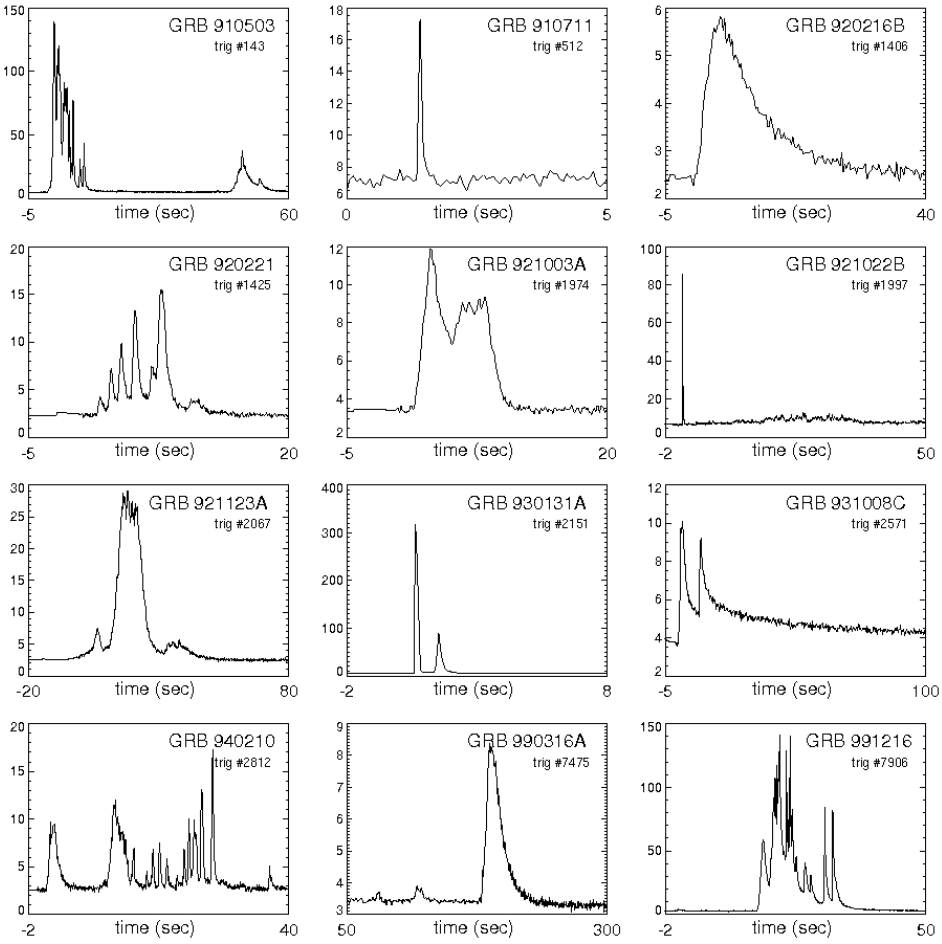

Figure 1.3: GRB lightcurves from BATSE showing the variability in the number of spikes, duration and countrates (Credit: NASA/BATSE)

Long duration GRBs

As the BeppoSAX first radio afterglow observation of GRB980425 had shown, there was a connection between long-duration GRBs and unusually bright supernovae. Today it is believed that long-duration GRBs are associated with core-collapsing massive stars in the order of 20-50$M_{\odot}$ (Hjorth & Bloom (2012)). This is also related to the formation of Black Holes (BH), or Neutron Stars (NS). This happens when the star has used all its fuel for energy generation by fusion in the core and then no longer can prevent gravitational collapse. For sufficiently massive cores not even the degenerate electron or neutron pressures can prevent collapse.

While the core of the star forms a black hole, the outer layers gets shed of and some of it ends up in rotation around the newly formed black hole and forms a so-called accreation disk. Complex electrical and magnetic fields then presumably form two jets in opposite directions along the stars rotational axis and ejects the material with ultra-relativistic speeds, plowing through the outer layers of the exploding star within tens of seconds. Collisions and shocks between material in the jets moving at different relativistic speeds is believed to give rise to the prompt emission in gamma-rays. When the jet further out

collide with material surrounding the collapsing star the afterglow is believed to form. This is the generic scenario believed to form long-duration GRBs.

Short duration GRBs

Short-duration GRBs have been much more elusive to understand due to their short duration bursts and weaker afterglows. The short durations makes them difficult to pin-point and locate accurately enough to obtain afterglow spectre and therefore more information about their properties and enviroments. However, it is believed that short-duration GRBs are the results of NS-NS or NS-BH mergers, where computer-simulations have shown that they occur on timescales of shorter durations than their long-duration counterparts (e.g., Rosswog et al. (2003)).

While the long-duration GRBs typically are found in bright regions in star-forming galaxies with increased probability of core-collapsing supernovae (Fruchter et al. (2006)), short-duration GRBs are typically observed in the outer regions of a broader mix of galaxies including quiescent galaxies (i.e. galaxies with old stellar populations) where NS-NS or BH-BH-mergers are more likely to occur (Berger (2014)). Observations of short-duration GRBs with no subsequent detection of supernovae in the afterglow supports this idea (Berger (2014)).

Long GRBs as probes

Having established that GRBs are the results of extreme collapse events that can be detected to very large distances due to their enormous released energies it was early on realised that long GRBs can be used as probes of the very distant Universe (Wijers et al. (1998)). Three examples of long GRBs as probes are: *i)* GRBs can help pin-point star-forming galaxies out to very large redshifts (the host galaxies) and hence help providing a characterization of the population of star-forming galaxies with a selection method that is complementary to more traditional flux-limited galaxy surveys (e.g., Fynbo et al. (2012)), *ii)* long GRBs can provide detailed information of chemical abundances along the lines of sight to massive stars (Fynbo et al. (2008)), and *iii)* GRBs can provide an independent measurement of the escape of ionizing radiation from galaxies (Chen et al. (2007)).

Chapter 2

Standard Cosmology

2.1 Introduction

In this chapter I wish to give a brief introduction to the overall cosmological model we use as a framework for understanding the types of data I have worked with in my thesis, i.e. spectra of very distant sources.

About 13.8 billion years ago our Universe started expanding from an initial hot phase - the Big Bang. Although the very early Universe at $t < 10^{-6}$s is still uncertain, the subsequent evolution of the Universe from a fraction of a few milliseconds $t \approx 10^{-5}$s all the way up to present day is reasonable and reliable well understood in what is known as the Hot Big Bang Model - also sometimes referred to as *Standard Cosmology*.

A full development of the standard cosmology is beyond the scope of this thesis (and how does one condense an entire history of cosmology into a short paper?). Nevertheless, to provide an introduction to the Universe we live in and the underlying cosmological framework, in which we interpret observations of phenomena as distant GRBs, I will present the origin of the light elements, the radiation from the initial fireball - the so-called CMB, the energy-density content, the evolution and expansion of the Universe as well as the formation of galaxies and large-scale structures.

2.2 Primordial nucleosynthesis

The events that took place in the very early stages of the Universe at the time-scales of a few minutes are referred to as the epoch of primordial nucleosynthesis where the temperature and density was high enough for the neutrons, protons, electrons, positrons and the neutrinoes to be in thermal equilibrium. As the temperature dropped below certain thresh-hold-values with the universal expansion, the first particles to "decouple" out of this plasma was the neutrinoes, at a temperature $T \approx 1 \times 10^{10}\,\mathrm{K}$ corresponding to approximately 1 sec. after the Big Bang. Theory predicts a neutrino background radiation much like the CMB at a present day temperature of $T = 2\,\mathrm{K}$ which is still not yet discovered.

Following the neutrino-freeze-out, the temperature and energy drops further to a level where photons can no longer produce pairs of positrons and electrons, so the electrons and positrons annihilate, leaving only the protons and neutrons from the original thermodynamical equilibrium. From statistical mechanics arguments one can show that the neutron to proton ratio at equilibrium was:

$$\frac{n}{p}_{eq} = e^{-(m_n - m_p)c^2/kT} = e^{-1.29\text{MeV/kT}} \tag{2.1}$$

where m_n and m_n is the neutron and proton mass and k the Boltzmann constant. Thus, approximately 1 sec. after the Big Bang where $T \approx 10^{10}\text{K} \Leftrightarrow kT \approx 0.8\text{MeV}$, this ratio was:

$$\frac{n}{p}(t = 1\text{sec}) \approx e^{-1.29/0.8} \approx 0.22 \tag{2.2}$$

With the half-life of the neutrons being $\tau \approx 300\,\text{s}$ the race towards building heavier atomic nuclei therefore had begun, before the temperature and density would reach values too low for any further nuclear reactions to take place. At the end of the primordial nucleosynthesis approximately 3 minutes after the Big Bang, the Universe consisted of hydrogen, helium and heavier elements with the relative mass abundances of:

$$(X, Y, Z) \approx (0.78, 0.22, 0) \tag{2.3}$$

The formation of heavier elements throughout the history of the Universe is hereafter attributed to the conversion of primordial hydrogen and helium in stars and star-forming galaxies. Fusion processes in the interior of stars gradually forms heavier and heavier elements, on different timescales and the end-result of starformation and evolution is a chemically enriched environment, when proto-stars end their lives as either white dwars, neutron stars, supernovae or black holes - depending on the mass of the proto-star.

2.3 The redshift-relation

The cosmological principle asserts that the Universe for a given moment in time looks the same everywhere i.e. that no region or direction of the Universe is special. It concerns the largest scales, thus one should imagine averaging over all the matter and energy present at smaller scales (e.g. stars, planets, dust, galaxies, clusters of galaxies, etc.) to find the average distribution of matter at the largest scales. According to the cosmological principle this averaged distribution of matter looks the same everywhere. [1]

Since the geometry of space-time is sourced by the matter (or rather energy and pressure collectively referred to as stress-energy), in the jargon of the theory of General Relativity, it follows that the geometry of the Universe at the largest scales should look the same everywhere for any given time. The cosmological principle naturally gives rise to the Robertson-Walker metric: See Carroll (2004)

[1] The smoothness of this average distribution of matter is observationally confirmed by galaxy-counts, however, the strongest evidence is from the CMB which has a constant temperature of around 2.7 K with very little variations of order 10^{-5} relative to this.

$$ds^2 = -dt^2 + a(t)\left(\frac{dr^2}{1-\kappa r^2} + r^2 d\Omega^2\right) \tag{2.4}$$

with the space-time coordinates (t, r, θ, ϕ) and $d\Omega^2 = d\theta^2 + \sin^2\theta d\phi^2$. The curvature parameter is $\kappa \in -1, 0, 1$ and the function $a(t)$ is the scale-factor.

The Robertson-Walker metric describes a homogeneous and isotropic Universe in which distances are allowed to expand (or contract) as a function of time, and the geometrical interpretation of the curvature parameter is those of an open, flat or closed Universe for $\kappa = -1, 0, +1$ respectively. From the Robertson-Walker metric one can show the cosmological redshift relation:

$$z = \frac{a(t_f) - a(t_i)}{a(t_i)} = \frac{a(t_f)}{a(t_i)} - 1 \tag{2.5}$$

Where $a(t_i)$ is the scale-factor at the (initial) time of emission of a lightray and $a(t_f)$ is the scale-factor at the (final) time of observation of a lightray. Setting the scale-factor to $a(t_f) = 1$ at the present time we get:

$$1 + z = \frac{1}{a(t_i)} \tag{2.6}$$

Thus, if we are observing a galaxy with a redshift $z = 2$ we are observing it as it was when the Universe had a scale factor $a(t_i) = \frac{1}{3}$. The cosmological redshift is hence a measure of how much the Universe has expanded between emission and observation of a lightray.

2.4 Evolution of the scale-factor

A description of the evolution of the scale-factor is based on the General Theory of Relativity and the Einstein equation, from which the Friedmann and the fluid equation can be derived.

Einsteins equation (and the geodesic equation) is the generalization of the Poisson equation in Newtonian mechanics and Newtons 2. law, to General Relativity popularized by the saying: "*stress-energy tells space-time how to curve, and curvature of space-time tells stress-energy how to move*".

The Friedmann and fluid equations are governing the behaviour and evolution of the scale-factor and can be written as:

$$\frac{\dot{a}^2}{a^2} = \frac{8\pi G}{3}\rho - \frac{\kappa}{a^2} \tag{2.7}$$

$$\dot{\rho} = -\frac{3\dot{a}}{a}(\rho + P) \tag{2.8}$$

where a is the scale-factor, ρ the total energy-density and P the pressure (Carroll (2004)).

Together with an equation of state relating the energy-density to the pressure, one has three equation in the three unknown functions, $a(t)$, $\rho(t)$ and $P(t)$ which can hence be solved. With the Hubble parameter and the critical density the Friedmann equation for a flat (or close to flat) Universe containing matter, radiation and dark-energy takes a particularly simple form:

$$\Omega = \Omega_m + \Omega_r + \Omega_\Lambda = 1 \tag{2.9}$$

where $\Omega_m = 0.31$, $\Omega_r = 8.4 \times 10^{-5}$ and $\Omega_\Lambda = 0.69$

In this composite model - the Benchmark Model of the Universe, with baryonic matter (B), radiation (R), dark matter (DM) and dark energy (Λ), the scaling relations are showed in Table 2.1

Table 2.1: Equation of state parameters, scaling, energy-density and present day density parameters for the Benchmark Model.

Component	ω	n	ρ	Ω
B	0	3	a^{-3}	0.05
DM	0	3	a^{-3}	0.26
R	$\frac{1}{3}$	4	a^{-4}	8.4×10^{-5}
Λ	-1	0	a^0	0.69

Using Table 2.1 its straightforward to calculate the present ratio of the energy-density of the dark energy to the energy-density of matter, where the subscript "0" emphasizes that it is the present values of the density parameter:

$$\frac{\Omega_{\Lambda,0}}{\Omega_{m,0}} = \frac{0.69}{0.31} \approx 2.2 \tag{2.10}$$

In the past when the scale-factor was smaller, the matter-Λ equality occurred at a time when the scale factor of the Universe was:

$$a_{m/\Lambda} = \left(\frac{\Omega_m}{\Omega_\Lambda}\right)^{1/3} \approx \left(\frac{0.31}{0.69}\right)^{1/3} \approx 0.77 \tag{2.11}$$

The present day ratio of the energy-density of the baryonic matter to the energy-density of radiation is:

$$\frac{\rho_{m,0}}{\rho_{r,0}} = \frac{\Omega_{m,0}}{\Omega_{r,0}} \approx \frac{0.31}{8.4 \times 10^{-5}} \approx 3600 \tag{2.12}$$

Similarly; the radiation-matter equality took place at a time when the scale factor was:

$$a_{r/m} = \frac{\Omega_r}{\Omega_m} \approx \frac{8.4 \times 10^{-5}}{0.31} \approx \frac{1}{3600} \approx 2.7 \times 10^{-4} \tag{2.13}$$

Since the Universe is monotonically expanding one can equally well express these unique moments in the history of the Universe in terms of the redshift using the redshift relation found in Eqn. 2.6. Converting the equation one therefore finds that the radiation-matter equality took place at a redshift of:

$$z = \frac{1}{a} - 1 \approx \frac{1}{2.7 \times 10^{-4}} \approx 3600 \tag{2.14}$$

Similarly, the matter-Λ equality took place at a redshift of:

$$z = \frac{1}{a} - 1 = \frac{1}{0.77} - 1 \approx 0.3 \tag{2.15}$$

The Universe was therefore radiation-dominated for $z > 3600$, matter-dominated in the range $3600 > z > 0.3$ and dark-energy dominated for $z < 0.3$. In addition to expressing the energy-density-equalities in terms of the scale-factor or the redshift, one can also compute the age of the Universe at the corresponding equalities. The radiation-matter equality therefore took place at a time when the Universe was:

$$t_{r/m} = 3.34 \times 10^{-6} H_0^{-1} \approx 47.000\text{yr} \tag{2.16}$$

Similarly, the transition from a matter-dominated to a Λ-dominated epoch took place at:

$$t_{m/\Lambda} = 0.702 H_0^{-1} \approx 9.8\text{Gyr} \tag{2.17}$$

The above discussion is following Ryden (2003).

2.5 The temperature relation

Since the Universe is expanding it must have been denser and hotter in the past at smaller scale-factors, or conversely at higher redshifts, so what we want is a relation between the temperature and the scale-factor or the redshift alternatively. Because the CMB is exquisitely well fitted by a blackbody spectrum with a temperature T_0, energy-density ρ_γ and pressure P_γ given by:

$$T_0 = (2.725 \pm 0.001)\,\text{K} \tag{2.18}$$

$$\rho_\gamma = \alpha T^4 \qquad P_\gamma = \rho_\gamma / 3 \tag{2.19}$$

one can use the laws of thermodynamics to derive the following simple relation for the temperature and the scale-factor. See Ryden (2003)

$$T(t) \propto a(t)^{-1} \tag{2.20}$$

Identifying the present day temperature T_0 of the CMB as $T_0 = 2.725\,\mathrm{K}$ and using the redshift relation Eqn. 2.6 one gets:

$$T(z) = 2.725\,\mathrm{K}(1+z) \tag{2.21}$$

The temperature of the CMB as the Universe expands is thus inversely proportional to the scale-factor, or alternatively; the temperature of the Universe is proportional to the redshift, such that when we look back in time, the Universe was hotter and hotter.

A very special moment in the history of the Universe was the decoupling of the photons as the temperature dropped below $T \approx 3000\,\mathrm{K}$ after which ions and electrons could combine to form neutral atoms. This moment is referred to as the recombination epoch and from Eqn. 2.21 this occurred at a redshift of $z = 1100$ corresponding to about 378.000 years after the Big Bang.

Ever since has the Universe been transparent to photons, being able to stream freely throughout the Universe, carrying the imprint and afterglow of the Big Bang itself - today observed as the CMB.

2.6 Formation of structure

The structures observed today, such as galaxies and clusters of galaxies are objects formed by an initial density perturbation and the actions of gravity over time. The average energy density, at a given time in a volume V, large in comparison to the object in which we are averaging is:

$$\overline{\rho}(t) = \frac{1}{V}\int_V \rho(\vec{r},t)d^3r \tag{2.22}$$

such that the dimensionless density fluctuation becomes:

$$\delta(\overline{r},t) = \frac{\rho(\overline{r},t) - \overline{\rho}(t)}{\overline{\rho}(t)} \tag{2.23}$$

Overdense and underdense regions therefore has a positive and negative density fluctuation respectively, with the minimum value $\delta = -1$ corresponding to an empty region, $\rho = 0$. To account for the structure and formation of it, one therefore has to account for arbitrarily high density fluctuations, comparing the critical energy to say that of a human:

$$\delta = \frac{1\times 10^3 \mathrm{kg}\ m^{-2}}{9.2\times 10^{-27}\mathrm{kg}\ m^{-2}} \approx 10^{29} \tag{2.24}$$

For very small density fluctuations, $\delta \ll 1$ the growth in amplitude, can be studied using linear perturbation theory, where a small density fluctuation in an otherwise static and homogeneous sphere causes the sphere to undergo a gravitational collapse. One can show that the density perturbations, under the influence of gravity grows exponentially with time (Houjun Mo (2010)):

$$\delta(t) = A_1 e^{t/t_{dyn}} + A_2 e^{-t/t_{dyn}}, \tag{2.25}$$

where A_1 and A_2 depend on the initial conditions of the sphere, and therefore serves as two integration-constants, and t_{dyn} is a characteristic dynamical time for collapse:

$$t_{dyn} = \frac{1}{(4\pi G\overline{\rho})^{1/2}} \tag{2.26}$$

The critical overdensity, and hence collaps, occurs at $\delta_{collaps} = 1.68$ regardless of a cosmology with or without dark-energy. (See Houjun Mo (2010)). After the initial linear-regime, the density fluctuations and perturbations grows and becomes non-linear at some point, eventually collapsing and condensing into galaxies and clusters of galaxies - what cosmologist today refer to as the "foamy" or filamentary structure of the Universe on the largest scales.

Chapter 3

Theory

3.1 Introduction to spectre

A very important method in astronomy is the study of the absorption lines from spectre of distant sources. Obtaining these spectre and studying the positions, widths and shapes of these absorption lines unlocks a wealth of information about the system in particular such as the redshift, the chemical composition, the ionization state, the temperature, the pressure and the density of the material. Analyzing the afterglow of a GRB can thus reveal information about the host galaxy, through the existence of absorbing lines, and the redshift of the GRB can be determined.

The origin of the absorption lines is a quantum mechanical effect and they correspond to the energy difference between ionization states of the material, such that light with this energy difference or more can get absorbed or Compton-scattered. One very important absorption line and easily identifiable in absorption line systems is the Lyman-α line corresponding to an energy difference of 10.2 eV stemming from the 2→1 transition in neutral hydrogen, which is also equivalent to $\lambda = 1215.67\,\text{Å}$. Combining this with Eqn. 2.6 yields:

$$\lambda_o = 1215.67\,\text{Å}(1+z) \tag{3.1}$$

hereby connecting the redshift with the observed wavelength of the Lyman-α transition.

3.2 Formation of spectral lines

Broadening mechanisms

Absorption line profiles are not sharply defined as a naive expectation would suggest, but instead show broadening features due to several effects which will be described briefly in the following.

Natural broadening

One broadening effect is the so-called natural broadening due to the uncertainties in the life-times of the quantum-mechanical states of the atoms or ions given by Heisenbergs

uncertainty principle:

$$\Delta E \cdot \Delta t > \frac{\hbar}{2} \tag{3.2}$$

so shorter lifetimes gives naturally broader lines and vice versa. Such a broadening effect results in a normalized ($\int \phi(\nu) d\nu = 1$) profile, written as:

$$\phi(\nu)_{12} = \mathcal{L}(\nu) \tag{3.3}$$

where

$$\mathcal{L}(\nu) \equiv \frac{1}{\pi} \left[\frac{\gamma}{(\nu - \nu_{12})^2 + \gamma^2} \right] \tag{3.4}$$

and $\gamma \equiv A_{21}/4\pi$ where A_{21} is the spontaneous transition coefficient in an atom with two energy levels 1 and 2. This is the Lorentz profile describing the shape of an absorption line dominated by natural broadening.

Doppler broadening

In addition to the natural broadening effect, thermal motion of the absorbing gas will result in a Doppler broadening simply because of the relative motion of the gas along the line of sight, the gas being Doppler shifted away and towards higher and lower frequencies respectively (or lower and higher wavelengths respectively). The observed frequency will be shifted by an amount:

$$\nu_o - \nu_e = -\frac{v}{c} \nu_a \tag{3.5}$$

where ν_a is the absorption frequency in the rest frame of the absorber, ν_o is the absorption frequency observer moving along with the general expansion of the Universe and v is the peculiar velocity of the absorbing atom projected along the line of sight, v being positive when the atom is moving away from the observer.

If the velocity distribution of the absorbing atom follows that of a Maxwell distribution, then the distribution becomes:

$$\mathcal{P}(v) dv = \frac{1}{\pi^{1/2} b} \exp\left(-\frac{v^2}{b^2} \right) dv \tag{3.6}$$

where b is the Doppler parameter related to the velocity dispersion of the gas, σ, by $b = \sqrt{2}\sigma$.. If the peculiar velocity of the gas is solely caused by thermal motion, the Doppler parameter is related to the velocity distribution through:

$$b = \sqrt{2}\sigma = \sqrt{\frac{2 k_B T}{m}} \tag{3.7}$$

where k_B is Boltzmans constant and T the gas temperature.

It is thus seen that the higher gas-temperature, the broader velocity distribution and therefore a wider absorption-line. In the case with a peculiar velocity caused by thermal motion only, the line profile becomes a Gaussian centered at the resonance frequency ν_{12}:

$$\phi_{12}d\nu = \frac{1}{\pi^{1/2}b_\nu}\exp\left[-\frac{(\nu-\nu_{12})^2}{b_\nu^2}\right]d\nu \tag{3.8}$$

with $b_\nu = \frac{v_{12}}{c}b$

3.3 Line profiles

Voigt Profiles

Combining the natural broadening and doppler broadening mechanisms one gets the convoluted absorption line-profile - the so-called Voigt profile:

$$\phi(\nu) = \int_{-\infty}^{\infty}\mathcal{L}\left[\nu\left(1-\frac{v}{c}\right)\right]\mathcal{P}(v)dv \tag{3.9}$$

Defining

$$A \equiv \frac{c}{b}\frac{\gamma}{\nu} \qquad ; \qquad B \equiv \frac{c}{b}\frac{\nu-\nu_{12}}{\nu}$$

The Voigt profile can be written as: Houjun Mo (2010)

$$\phi(\nu) = \frac{1}{\sqrt{\pi}}\frac{c}{b}\frac{\mathcal{V}(A,B)}{\nu} \tag{3.10}$$

where

$$\mathcal{V}(A,B) = \frac{A}{\pi}\int_{-\infty}^{\infty}\frac{\exp\left(-y^2\right)^2}{(B-y)^2+A^2}$$

is called the Voigt function.

An approximation to the Voigt function is also given by Houjun Mo (2010):

$$\mathcal{V}(A,B) \approx \exp -B^2 + \frac{1}{\sqrt{\pi}}\frac{A}{A^2+B^2} \tag{3.11}$$

which shows that near the center of the absorption line the profile is dominated by the thermal broadening $B \ll 0$, while at the wings where $|\nu-\nu_{12}|/\nu_{12} \ll b/c \Leftrightarrow B \ll 1$ the profile gets dominated by a Lorentzian profile. The frequency intervals, in which natural broadening dominates thermal Doppler broadening, are called the damping wings of the line profile.

3.4 Line widths

Equivalent widths and column densities

An absorption line has an equivalent width, ω measured in [Å] defined as:

$$\omega_{obs} = \frac{I_c - I}{I_c} d\lambda = \int (1 - e^{-\tau(\lambda)}) d\lambda \tag{3.12}$$

where I is the observed spectral intensity, I_c the interpolation of the absorptionfree continuum over the absorption feature and $\tau(\lambda)$ the optical depth, a measure of how much of the light that gets absorbed when travelling through a medium. For redshifted absorption lines $\omega_o = \omega_e \times (1+z)$ since the equivalent widths gets redshifted too due to the universal expansion. Here ω_o and ω_e is the observed and emitted (in the rest frame) equivalent width respectively.

The optical depth can be related to the column density:

$$\tau(\lambda) = \int n(l)\sigma\lambda dl = \mathrm{N}\sigma(\lambda) \tag{3.13}$$

where the integration is over the path of the absorbing gas, $n(l)$ is the number-density of absorbing ions, N the column density and σ the absorbing cross-section.

The curve of growth method

For a Voigt profile one can relate the optical depth, τ to the column density N by:

$$\tau(\lambda) = \mathrm{N}\sigma_{12} = \eta_0 \mathcal{V}(A, B) \tag{3.14}$$

where

$$\eta_0 \equiv \frac{1}{\sqrt{\pi}} \frac{c}{b} \frac{a_{12}}{\nu_{12}} \mathrm{N}$$

Plotting the equivalent width ω, as a function of the column density N, or more specifically ν_0, gives the so-called curve-of-growth. For a given species of absorbing atoms this curve relates ω with N and the Doppler parameter. The theoretical curve-of-growth falls in 3 different optically depth regions:

Optically thin regime

For $\eta_0 \leq 1$ the optical depth is small and the equivalent width reduces to:

$$\omega \simeq \int_0^\infty \tau(\lambda) d\lambda = \frac{a_{12}}{\nu_{12}} \lambda_{12} \tag{3.15}$$

In this case the equivalent width increases linearly with the column density, independent of the b parameter. The relation is:

$$\mathrm{N} = \frac{W}{\lambda} \frac{1.1 \times 10^{20} \mathrm{cm}^{-2}}{f\lambda[\text{Å}]^2} \tag{3.16}$$

This relation also determines a lower limit to the column density once the equivalent width has been measured.

Intermediate regime

The line profile is dominated by thermal broadening and becomes optically thin near the line center. The equivalent with increases very slowly with increasing column density and is dependent on the b-parameter. The line gets saturated with increasing b and the relation is:

$$\omega \approx \frac{2\mathrm{b}}{\nu_{12}}\sqrt{ln(\eta_0)} \tag{3.17}$$

or

$$\omega \propto \sqrt{ln(N)} \tag{3.18}$$

There is thus a degeneracy in the intermediate regime where one cannot distinguish between optically thick absorption lines and high Doppler parameters. Assuming a lower limit for the column density one can fit for various Doppler-parameters. This will be shown for selected metal lines in the next chapter.

Optically thick regime

At the optical thick region the curve-of-growth becomes independent of the b-parameter again, and the line gets saturated. For $\eta_0 \leq 10^4$ the equivalent width can be written as:

$$\omega \simeq \lambda_{12} x_0 \int_{x_0^{-1}}^{\infty} \left[1 - \exp\left(-y^{-2}\right)\right] dy \tag{3.19}$$

with

$$x_0^2 = \frac{2}{3\pi}\left(\frac{a_{12}}{\nu_{12}}\right)^2 \frac{N}{\lambda_{12}}$$

and it can be shown that: (see Houjun Mo (2010))

$$\omega \propto \sqrt{N} \tag{3.20}$$

Figure 3.1, adapted from Petitjean (1998) shows curve of growths for various values of the Doppler parameter in the different optically thin, intermediate and thick regimes. It is clear from the figure that there is no dependency on the b-parameter in the optically thin and thick regimes - also called the damped wings, while for the flat part of the curve of growth, i.e. the intermediate regime the equivalent width grows with increasing b. The relations for the different parts of the curve-of-growth is given by Eqn. 3.16, 3.18 and 3.20 respectively.

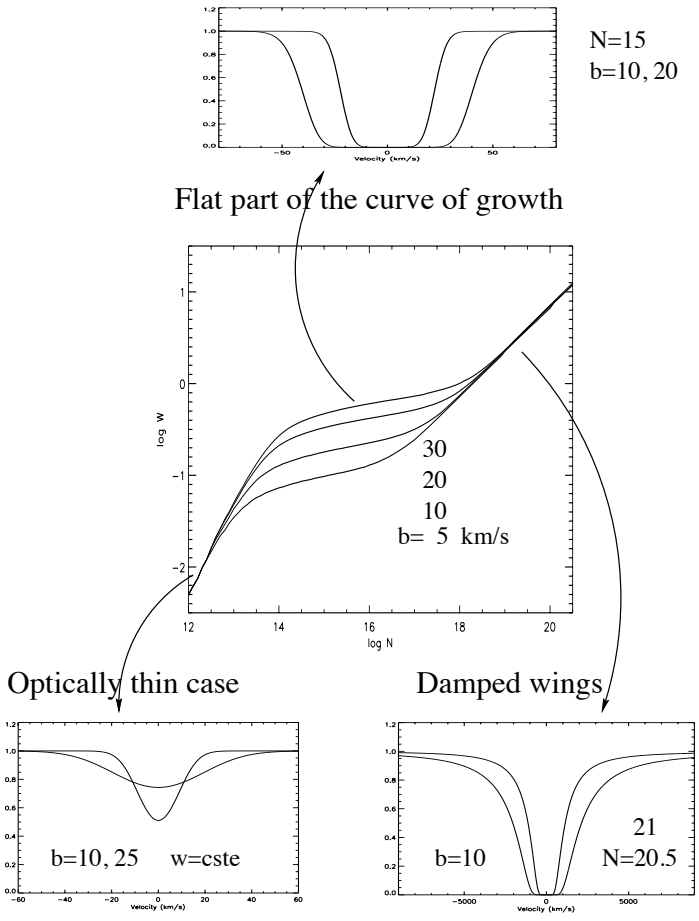

Figure 3.1: Curve-of-growth and the relation between column density and equivalent width for different optical regimes (from Petitjean (1998)). The three inserts show the three different regimes: optically thin lines, the flat part of the Curve of growth with saturated lines, and finally lines that are saturated in the damping wings.

Chapter 4

Analyis of the GRB151021A spectrum

4.1 The Data

At 01:29:12 UT, 21. October 2015 the Swift Burst Alert Telescope (BAT) was triggered by an event with countrates at around 2500 counts/sec and started immediately to slew towards the burst now known as GRB151021A (Melandri et al. (2015)). On board calculations revealed the location to be:

$$\text{RA(J2000)} = \text{22h 30m 27s}$$
$$\text{Dec(J2000)} = \text{-33d } 11'55''$$

with an uncertainty of 3 arcmin. The XRT began observing the field at 01:30:43.2 UT, 90.7 seconds after the BAT trigger and found a bright uncataloged X-ray source located at:

$$\text{RA(J2000)} = \text{22h 30m 35.09s}$$
$$\text{Dec(J2000)} = \text{-33d } 11'56.7''$$

with an uncertainty of 3.6 arcseconds. This location was 106 arcseconds off from the BAT onboard positioning, but within the BAT error circle. A power-law fit to the X-ray afterglow spectrum gave a column destiny in excess of the galactic value $1.13 \times 10^{20} \text{cm}^{-2}$.

Follow-up observations with the X-shooter at the VLT (Paranal Observatory, Chile) started at 02:13 UT (44 min after the burst) and covered a range between 3000Å and 24800Å. The X-Shooter detected a bright uncataloged object in the r-band, in close proximity of the XRT error circle at coordinates (de Ugarte Postigo et al. (2015)):

$$\text{RA} = \text{22:30:34.369}$$
$$\text{Dec} = \text{-33:11:49.45}$$

The authors suggest this is the optical afterglow of GRB 151021A and after preliminary reduction of the obtained data, they report absorption features of SII, OI, SiII, SiIV, CIV, AlII, ZnII, CrII, FeII, NiII, MnII, MgII, MgI as well as fine-structure lines from FeII* and NiII*. The Lyman-alpha absorption line is identified at a common redshift of $z = 2.33$ and in addition there is an intervening system at $z = 1.49$ featuring lines of FeII, MgII and MgI.

4.2 Determining the redshift

From the localization of the Lyman-α line in the obtained spectrum, one can easily calculate the redshift according to Eqn. 2.6

$$z = \frac{4050\text{Å}}{1215.67\text{Å}} - 1 \approx 2.33 \tag{4.1}$$

Using the identified lines from the spectrum in the UVB-band and VIS-band, and using the rest-frame wavelength of the corresponding lines, kindly provided by Johan P. U. Fynby, in the atompar.dat file, one can identify all the lines in the spectrum and derive a more precise value of the GRB redshift.

This has been done in Table 4.1 listing the lines in the UVB-band redwards of the Lyman-α line, and Table 4.2 showing the lines identified in the VIS-band part of the spectrum respectively. This line identification has constituted a large part of my work in the thesis. The challenge is to identify all the lines. This would be more simple if there were only lines from the GRB host galaxy in the spectrum, but there are also absorption lines from other absorption systems along the line of sight. These are in the literature referred to as intervening absorption systems and they are well known from studies of quasar absorption line systems (e.g., Weymann et al. (1981)).

In the spectrum I identify intervening absorption systems at $z = 1.972$ (CIV) and $z = 1.491$ (many metal lines). For some of the lines I am unsure about the identification (e.g., the TiII-3242 line, which is uncommon). There may hence be other intervening systems along the line of sight.

The GRB redshift is determined to be $z = 2.3305 \pm 0.0005$ and the intervening system at a redshift around $z = 1.49$ is evident.

Using IDL one can measure an equivalent width and its uncertainty for each line. This is showed in the last column of Table 4.1 and Table 4.2, with an example output given in Figure 4.1.

4.3 DLA fitting

To obtain a measure of the HI column density, the Damped Lyman-α (DLA) line is used and fitted with the column density as a free parameter, using an IDL-script. This script uses the approximation described in Tepper-García (2006). The best obtained fit is shown in Figure 4.2, including the Lyman-β-line also visible in the spectrum. This is also a check of consistency, the DLA absorption lines for Lyman-α and Lyman-β are exactly where they should be. The obtained column density for this DLA fit is $N_{HI} = 1.2 \times 10^{22}\text{cm}^{-2}$ approximately two orders of magnitude larger than the galactic value.

Table 4.1: UVB lines in the spectrum of the afterglow of GRB151021A

λ_{obs}[Å]	Line Id	z	ω[Å]
4160.85	AlII-1670	1.497	1.25± 0.23
4164.06	SII-1250	2.331	1.08± 0.21
4175.02	SII-1253	2.332	1.74± 0.25
4194.20	SII-1259	2.331	2.08± 0.28
4196.70	SiII-1260	2.331	2.68± 0.30
4211.22	SiII*1264 SiII*1265	2.330	1.90± 0.23
4335.96	OI-1302	2.330	3.07± 0.18
4343.32	SiII-1304	2.331	2.82± 0.17
4359.32	SiII*-1309	2.330	0.83± 0.13
4385.65	NiII-1317	2.330	0.86±0.10
4443.11	CII-1334	2.331	3.79±0.18
4562.09	NiII-1370	2.330	1.08±0.13
4601.70	CIV-1548	1.972	1.85±0.11
4609.30	CIV-1550	1.972	1.67±0.11
4618.97	AlIII-1854	1.491	0.99±0.09
4640.38	AlIII-1862	1.492	3.07±0.13
4670.85	SiIV-1402	2.332	1.92±0.11
5083.33	SiII-1526	2.331	2.86±0.11
5105.81	SiII*-1533	2.331	1.24±0.10
5120.63	CrII-2056	1.491	0.61±0.08
5136.01	CrII-2062 + ZnII-2062	1.491	0.92±0.11
5145.45	CrII-2066	1.491	0.39±0.10
5156.81	CIV-1548	2.331	3.20±0.15
5163.23	CIV-1550	2.331	2.82±0.12
5355.49	FeII-1608	2.331	2.43±0.09
5364.49	FeII-1611	2.330	0.59±0.07

4.4 Column densities

Because of the linear relation between the equivalent width and the column density as expressed in Eqn. 3.16 in the optically thin regime, its possible to determine a lower limit to the column densities of the different ions. Table 4.3 is a summary of the lower limits to the column densities.

Its important to bear in mind that these column densities are lower limits assuming the optically thin regime. In reality the column densities should be larger than this, which will be examined using an effective b-parameter fitting in the next section.

4.5 Effective b-parameter fitting

Using several values of the equivalent widths for different lines with different oscillator strengths from a particular element, one can try to provide a better estimate for the

Table 4.2: VIS lines in the spectrum of the afterglow of GRB151021A

λ_{obs}[Å]	Line Id	z	ω[Å]
5603.96	FeII-2249	1.492	0.79±0.18
5630.19	FeII-2260	1.491	0.96±0.16
5691.31	NiII-1709	2.330	0.79±0.14
5799.93	NiII-1741	2.331	1.07±0.16
5833.23	NiII-1751	2.331	0.87±0.13
5839.74	FeII-2344	1.491	2.00±0.15
5896.95	NiII-1773	2.326	0.06±0.08
5913.96	FeII-2374	1.491	1.87±0.16
5935.76	FeII-2382	1.492	2.25±0.17
6021.98	SiII-1808	2.331	2.09±0.14
6175.97	AlIII-1854	2.331	2.51±0.20
6202.74	AlIII-1862	2.331	2.09±0.15
6417.62	MnII-2576	1.491	1.02±0.12
6441.79	FeII-2586	1.491	2.09±0.11
6461.34	MnII-2594	1.491	0.90±0.09
6475.52	FeII-2600	1.491	2.45±0.10
6491.03	MnII-2606	1.491	0.77±0.08
6746.60	ZnII+CrII+CoII-2026	2.330	2.07±0.09
6846.61	CrII-2056	2.330	1.22±0.08
6869.59	CrII+ZnII-2062	2.332	4.44±0.16
6879.60	CrII-2066	2.330	0.97±0.08
6964.18	MgII-2796	1.491	3.19±0.12
6982.00	MgII-2803	1.491	2.87±0.11
7105.12	MgI-2852	1.491	1.47±0.07
7491.45	FeII-2249	2.331	1.10±0.07
7527.70	FeII-2260	2.331	1.44±0.08
7805.77	FeII-2344	2.330	3.92±0.08
7906.37	FeII-2374	2.330	3.25±0.12
7934.55	FeII-2382	2.331	4.33±0.11
8076.31	TiII-3242	1.491	0.79±0.06
8580.22	MnII-2576	2.331	2.00±0.06
8612.95	FeII-2586	2.331	4.17±0.07
8639.02	MnII-2594	2.330	1.80±0.07
8657.47	FeII-2600	2.330	5.47±0.12
8678.86	MnII-2606	2.330	1.62±0.07

column density fit for an effective b-parameter. Below are the results of such a fit for the effective b-parameter for the lines SII, SiII, NiII, FeII and MnII respectively. This approach assumes that the total absorption profile can be approximated by a single Voigt-profile, it is therefore not a correct physical model for the absorption, but a step ahead relative to the lower limit from weak lines.

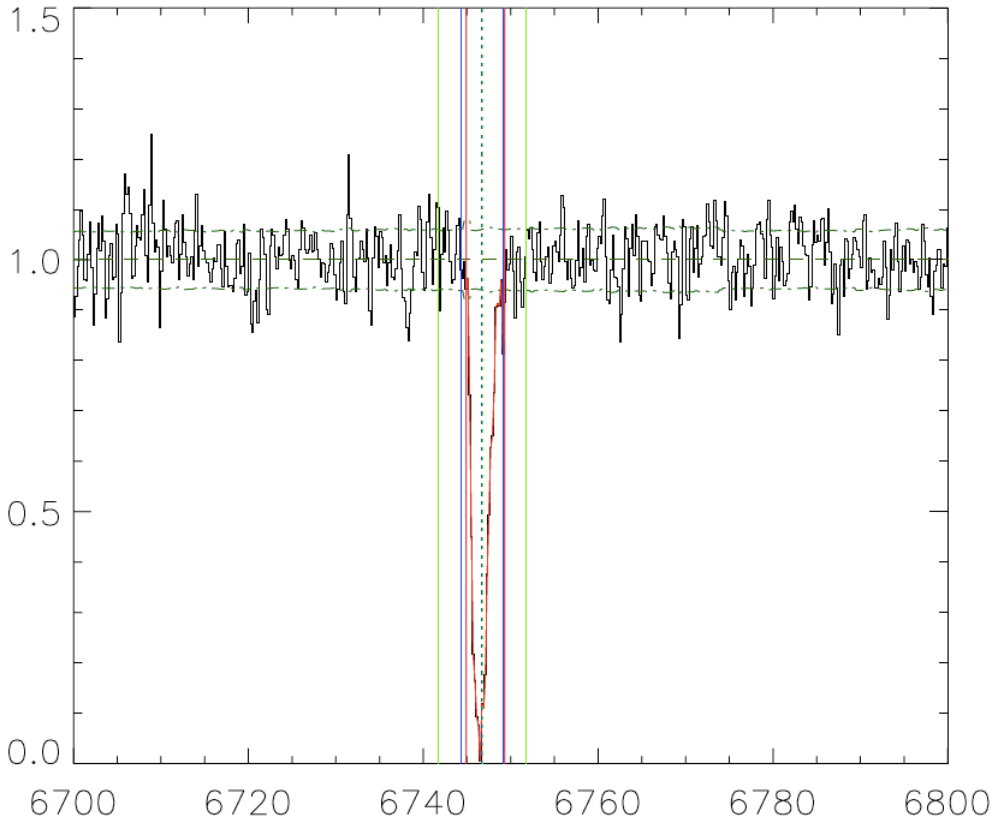

Figure 4.1: IDL fitting for the $\lambda_o = 6746.60$Å absorption line, which is a blend of lines from ZnII, CrII and CoII.

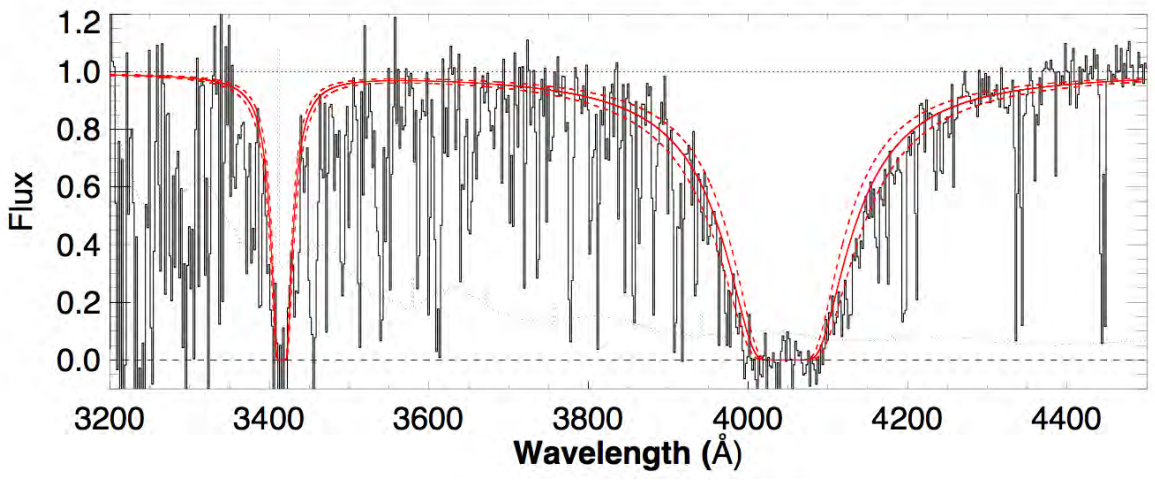

Figure 4.2: Fitting the column density of the DLA and the Lyman-β line.

Figure 4.3 shows the theoretical curve-of-growth for several values of the b-parameter and the 3 data points corresponds to the 3 SII lines found in Table 4.1. The assumed column density is $\log N = 15.62$ as seen from Table 4.3 and a b-parameter of $b = 35\,km/s$ fits best. There is a reasonable uncertainty to this coming from the fact that the points can be shifted, through a shift parameter given in the IDL-fit. We do not derive a formal

Table 4.3: Column density lower limit of selected weak lines

Ion	λ_e[Å]	λ_{obs}[Å]	ω[Å]	Lower limit for log N
SII	1250	4163	1.08±0.21	15.62±0.09
FeII	1611	5365	0.59±0.07	15.73±0.05
SiII	1808	6022	2.09±0.14	16.00±0.03
NiII	1773	5905	0.06±0.08	14.20±0.20
NiII	1317	4386	0.86±0.10	14.05±0.05
AlIII	1862	6201	2.09±0.15	13.85±0.03
CrII	2066	6881	0.97±0.08	14.20±0.04
MnII	2594	8639	1.80±0.07	13.50±0.02

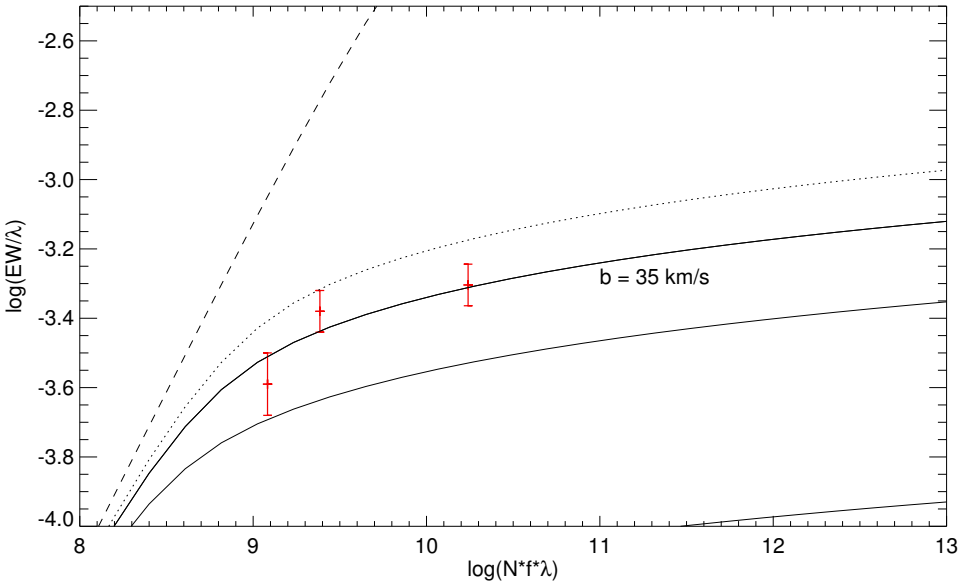

Figure 4.3: SII-line effective b-parameter fitting.

χ^2 fit, as this fit is only an indicative fit illustrating how much higher the abundances may be, than the lower limits derived from the assumption that the weak lines in Table 4.3 are optically thin. The shifting parameter for the SII-line has been set to 0.63.

Figure 4.4 shows the same IDL programming routine now for the 4 SiII-lines found in Table 4.1. The assumed column density is $\log N = 16.60$ and the effective b-parameter of $b = 35\,km/s$ is a good fit. The uncertainty is again somewhat large trying to optimize the shifting parameter for the best fit. The shifting parameter for this SiII-line has been set to 0.6

The lower limit column density of $\log N = 14.05$ and $b = 35\,km/s$ also matches for the Ni-II and Fe-II line as seen from Figure 4.5 and Figure 4.6 respectively with shifting parameters of 0.7 and 0.065 for Ni-II and Fe-II.

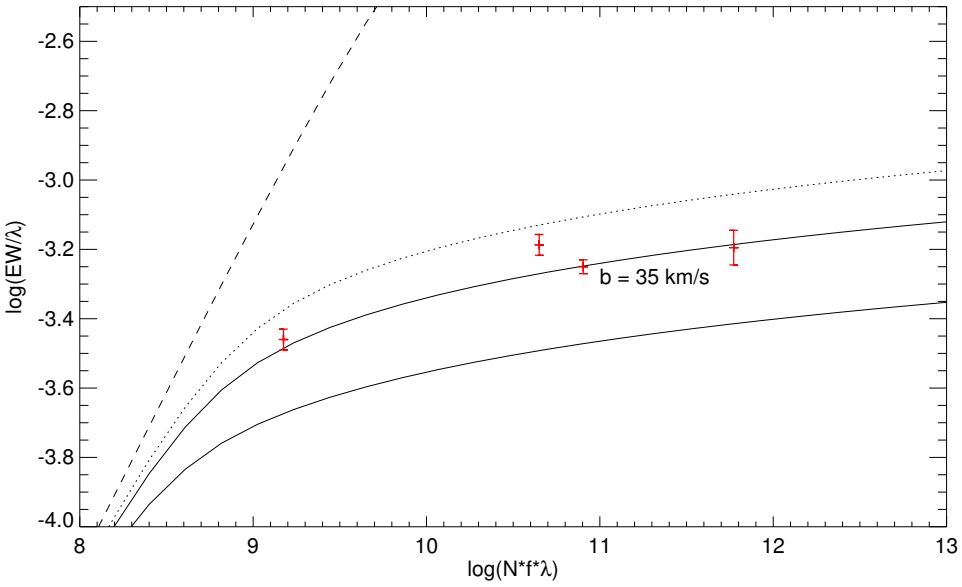

Figure 4.4: SiII-line effective b-parameter fitting

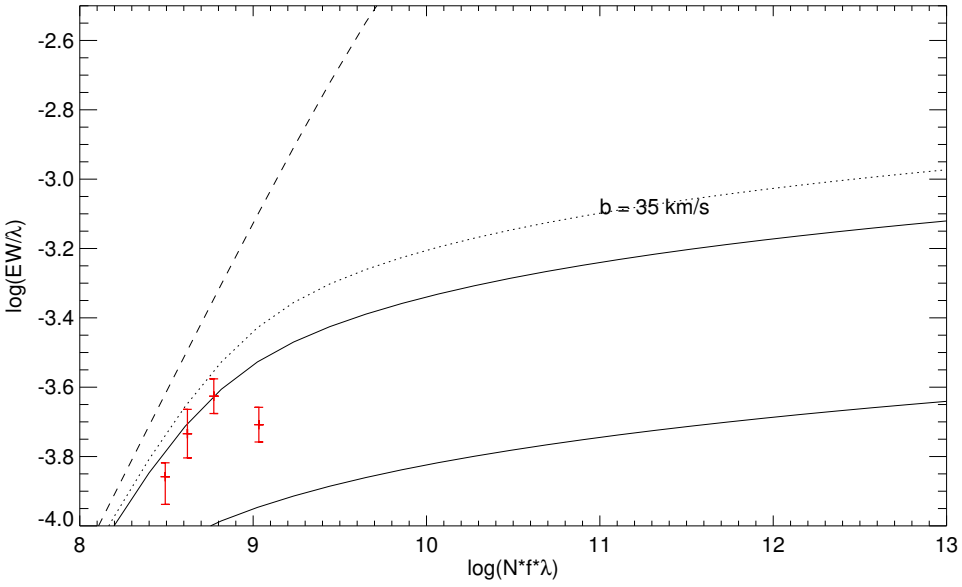

Figure 4.5: NiII-line effective b-parameter fitting

The data-point corresponding to the NiII-1317 line with $\omega = 0.86$ in Figure 4.5 is not fitting well with the rest of the data, for reasons unknown. The equivalenth width is too low.

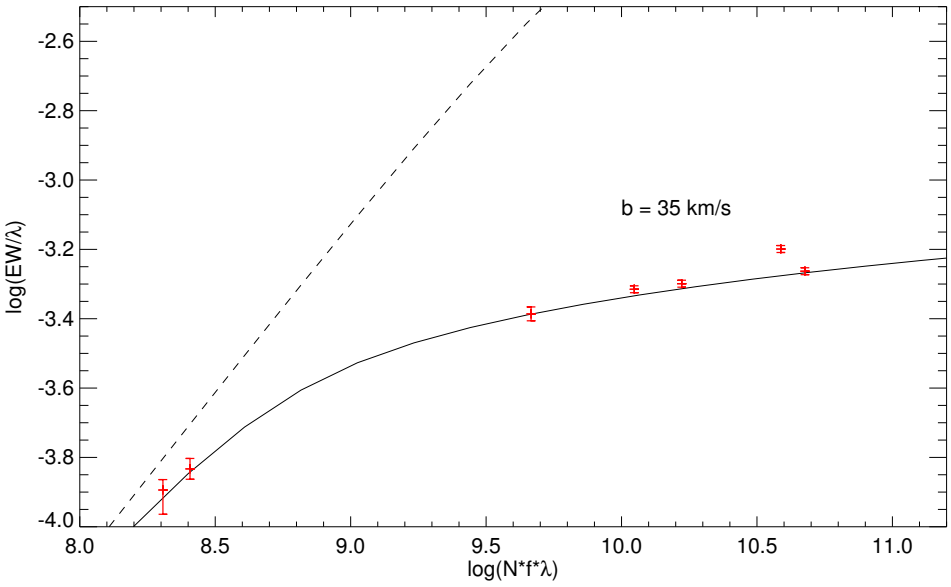

Figure 4.6: FeII-line effective b-parameter fitting

With the shifted parameters the new column densities and better fits now becomes. See Table 4.4:

Table 4.4: Column densities of selected ions using effective doppler parameter fits.

Ion	λ_e[Å]	λ_{obs}[Å]	ω[Å]	log(N)
SII	1250	4163	1.08±0.21	16.25±0.09
FeII	1611	5365	0.59±0.07	15.80±0.05
SiII	1808	6022	2.09±0.14	16.60±0.03
NiII	1773	5905	0.06±0.08	14.90±0.20
NiII	1317	4386	0.86±0.10	14.75±0.05

4.6 Metallicity and relative abundances

The metallicity (or the abundance ratio) is defined as the logarithm of the metallicity compared to that of the Sun, i.e.

$$[A/H] = \log\left(\frac{N_A}{N_H}\right) - \log\left(\frac{N_{A,\odot}}{N_{H,\odot}}\right) \tag{4.2}$$

where the solar abundances are taken from Asplund et al. (2009).

Table 4.5 summarizes the obtained metallicity measurements.

Table 4.5: Metallicities of selected elements

Element	$\log\left(\frac{N_A}{N_H}\right)$	$\log\left(\frac{N_{A,\odot}}{N_{H,\odot}}\right)$	$[A/H]$	Solar abundance
SII	-5.83	-4.88	-0.95	0.112
FeII	-6.28	-4.50	-1.78	0.017
SiII	-5.48	-4.49	-0.99	0.102
NiII	-7.18	-5.78	-1.40	0.004
NiII	-7.33	-5.78	-1.55	0.003

The reason why FeII and NiII give low values for the metallicity is most likely due to depletion onto dust graines (De Cia et al. (2013)). Some elements, referred to as volatiles, deplete strongly onto interstellar dust, iron and nickel are volatiles. Other elements, such as sulpher and zink, deplete much less onto dust (so-called refractory elements). The sulpher-based metallicity of -0.95 is therefore my best estimate of the metallicity of the host galaxy.

4.7 Host galaxy search

Knowing the redshift of the GRB one can start searching for the host galaxy emission lines. Usually one looks for the bright [OIII]-5006.843 line which will be redshifted to the NIR part of the spectrum, in this case to:

$$\lambda_o = (1 + 2.33) \times 5006.843\text{Å} \approx 16673\text{Å} \tag{4.3}$$

By subtracting the GRB spectrum in the NIR region of the redshifted oxygen line, its possible to identify the host galaxy [OIII] emission line. See Figure 4.7

An IDL fitting procedure determines the center of the emission-line, the line-width and the amplitude. The center of the emission line is found to be at: $\lambda_c = 16677.4$Å with an equivalent line width of $\sigma = 5.1$ Å. Figure 4.8 is the output plot of the [OIII] emission line from the IDL-fit. The emission line redshift of the galaxy is hence $z = 16677.4/5006.843 - 1 = 2.3309$.

This is very close to the absorption line redshift, e.g. from the SiII-1808 line where I find $z = 6021.98/1808.0126 - 1 = 2.3307$ or a difference of only $v = 0.0002/3.3309 * c = 18$

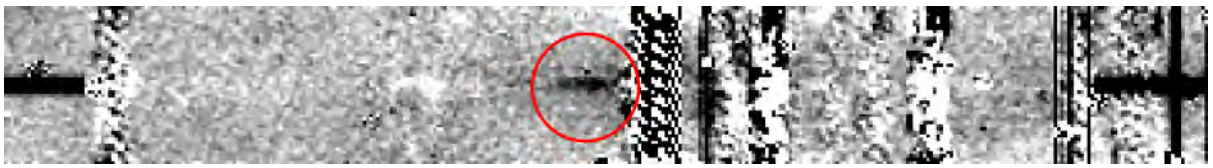

Figure 4.7: The [OIII]-5006.843 line showing in the subtracted spectrum in the NIR region

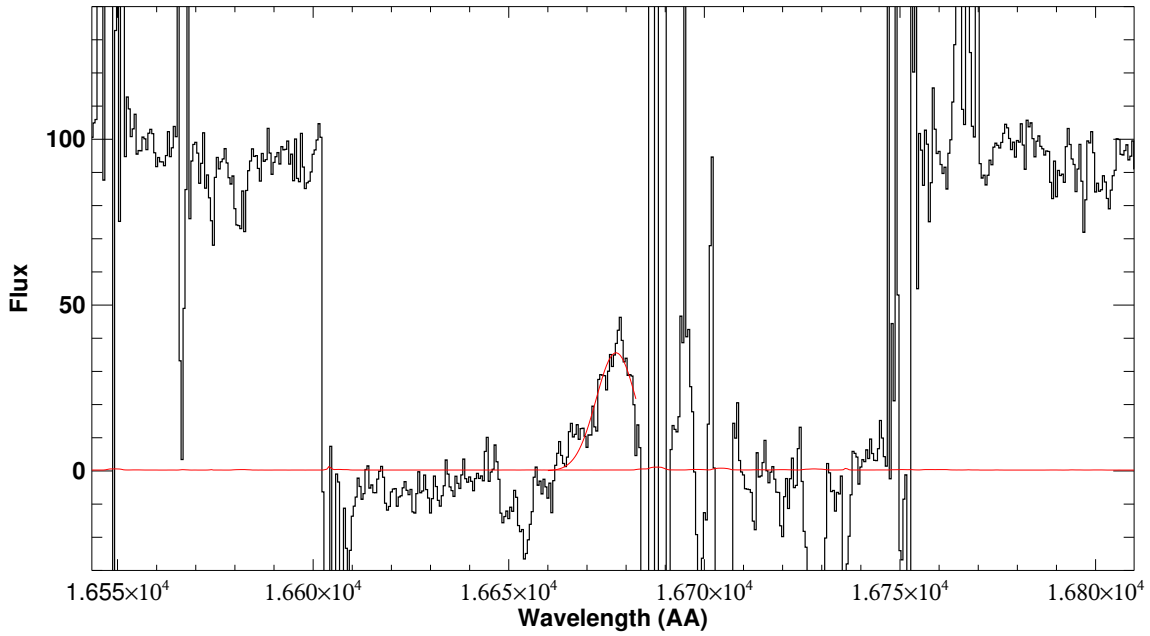

Figure 4.8: The [OIII] emission line.

km s^{-1}.

This means that the sightline to the GRB progenitor location most likely probes the central region of the galaxy. For comparison the width of the [OIII] emission line is 5.1 Å, corresponding to a full-width-at-half-maximum of 240 km s^{-1}. Correcting for the spectral resolution, the true line width becomes somewhat lower - probabaly closer to about 180 km s^{-1}, which is still much larger than the offset between the emission line and absorption line redshifts.

Chapter 5

Results and Conclusion

Since the beginning of the afterglow era of GRBs in 1997 they have become a very important probe of star-forming galaxies at high-redshift due to their bright afterglows within an host galaxy, because there is a strong connection between long-duration GRBs and massive stars.

In the past two decades, however, there has been a remarkable increase in observational methods for locating high-redshift ($z > 2$) galaxies selecting different classes with different approaches e.g. Ly-α emitters, Lyman break galaxies, distant red galaxies, damped Ly-α systems, extremely red objects, long-duration GRB host galaxies, MgII absorbers, radio galaxies, quasar host galaxies etc. etc.

Of all the various techniques two methods offer the opportunity to study the interstellar medium at a precision comparable to the galaxy and its neighbours - the damped Ly-α systems intervening quasar sight lines (QSO-DLA) and the host galaxies of long-duration GRBs which exhibit bright afterglows (GRB-DLA).

The aim of all these techniques including GRB-DLA is to probe the processes of galaxy formation in the very young Universe and trace the cosmic chemical enrichment history, from the first metal-free objects such as Population III stars to the present day Universe.

In my thesis I have analysed a GRB-DLA. I have analysed the spectrum of GRB151021A and inferred the column densities for hydrogen and a number of metals and hence derived the metallicity for the host galaxy at a redshift of $z = 2.331$. This constitutes a new data-point in the growing sample of GRB afterglows observed in the past decades.

One recent sample of GRB-DLA metallicity measurements is presented by Cucchiara et al. (2015), the largest publicly available investigating the metallicities of long GRB hosts in the $z = 1.8 - 6$ range.

The metallicity for GRB151021A found to be $[X/H] = -0.95$ for SII and $[X/H] = -0.99$ for SiII is seen to fall in the upper half of previous measurements at similar redshifts in Figure 5.1. The fact that we detect the underlying host galaxy in the [OIII] emission

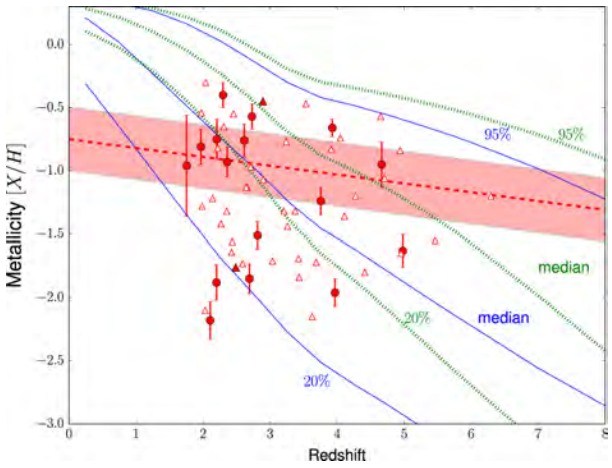

Figure 5.1: Metallicity-redshift distribution for a sample of GRB-DLAs at a specific reshift.

line is consistent with the expectation from the simple model presented in Fynbo et al. (2008). In this model it is assumed that high-z galaxies follow Luminosity-metallicity relations similar to galaxies in the local Universe such that galaxies with higher metallicities tend to reside in more luminous galaxies. See Figure 5.2. Even though I only detect the galaxy in the [OIII] emission line, the strength of the line makes it likely that the host galaxy probably is relatively luminous.

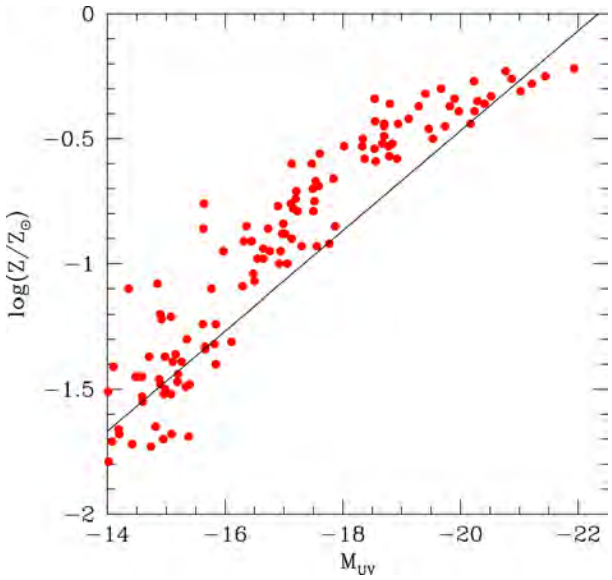

Figure 5.2: The metallicity/luminosity relation adopted in Fynbo et al. (2008) to model the metallicity distribution of GRB host galaxies.

In conclusion, I have derived the metallcity for the galaxy hosting GRB151021A at a redshift of $z = 2.33$. The galaxy metallicity as measured from SII lines is about 10% of the solar metallicity. Compared to similar measurements for other GRB host galaxies this is in the upper half of the measured metallicities.

I also detect the [OIII] emission line from the host galaxy indicating that the galaxy is probably relatively luminous. This is consistent with previous results finding a scaling relation between metallicity and luminosity for galaxies also at high redshifts.

Bibliography

Asplund, M., Grevesse, N., Sauval, A. J., & Scott, P. 2009, Annual Review of Astronomy and Astrophysics, 47, 481

Berger, E. 2014, Annual Review of Astronomy and Astrophysics, 52, 43

Carroll, S. M. 2004, An Introduction to Generel Relativity Spacetime and Geometry, ed. L. G. Adam Black, Nancy Benton (Pearsson)

Chen, H.-W., Prochaska, J. X., & Gnedin, N. Y. 2007, Astrophysical Journal, Letters, 667, L125

Costa, E., Frontera, F., Heise, J., et al. 1997, Nature, 387, 783

Cucchiara, A., Fumagalli, M., Rafelski, M., et al. 2015, Astrophysical Journal, 804, 51

De Cia, A., Ledoux, C., Savaglio, S., Schady, P., & Vreeswijk, P. M. 2013, Astronomy and Astrophysics, 560, A88

de Ugarte Postigo, A., Malesani, D., & Xu, D. 2015, GRB Coordinates Network, 18426

Frail, D. A., Kulkarni, S. R., Nicastro, L., Feroci, M., & Taylor, G. B. 1997, Nature

Fruchter, A. S., Levan, A. J., Strolger, L., et al. 2006, Nature, 441, 463

Fynbo, J. P. U., Malesani, D., & Jakobsson, P. 2012, Long Gamma-Ray Burst Host Galaxies and their Environments, Cambridge University Press, p. 269–301

Fynbo, J. P. U., Prochaska, J. X., Sommer-Larsen, J., Dessauges-Zavadsky, M., & Møller, P. 2008, Astrophysical Journal, 683, 321

Galama, T. J., Vreeswijk, P. M., van Paradijs, J., et al. 1998, Nature

Gehrels, N., Ramirez-Ruiz, E., & Fox, D. B. 2009, Annual Review of Astronomy and Astrophysics, 47, 567

Hjorth, J. & Bloom, J. S. 2012, The Gamma-Ray Burst - Supernova Connection, Cambride University Press, p. 169–190

Houjun Mo, Frank van den Bosch, S. W. 2010, Galaxy Formation and Evolution (Cambridge University Press, New York)

Melandri, A., Barthelmy, S. D., D'Avanzo, P., et al. 2015, GRB Coordinates Network, 18425

Petitjean, P. 1998, ArXiv Astrophysics e-prints [eprintastro-ph/9810418]

Rosswog, S., Ramirez-Ruiz, E., & Davies, M. B. 2003, Monthly Notices of the Royal Astronomical Society, 345, 1077

Ryden, B. S. 2003, Introduction to Cosmology, ed. J. M. Adam Black, Nancy Benton (Addison Wesley, 1301 Sansome St., San Francisco, CA 94111)

Tepper-García, T. 2006, Monthly Notices of the Royal Astronomical Society, 369, 2025

Thöne, C. C. 2008, Gamma-Ray Burst Host Galaxies at High Resolution (Faculty of Science, University of Copenhagen)

Weymann, R. J., Carswell, R. F., & Smith, M. G. 1981, Annual Review of Astronomy and Astrophysics, 19, 41

Wijers, R. A. M. J., Bloom, J. S., Bagla, J. S., & Natarajan, P. 1998, Monthly Notices of the Royal Astronomical Society, 294, L13